PHYSICAL REVIEW B **73**, 184125 (2006)

Explosive crystallization in the presence of melting

C. Grigoropoulos,[1] M. Rogers,[1] S. H. Ko,[1] A. A. Golovin,[2] and B. J. Matkowsky[2]
[1]*Department of Mechanical Engineering, University of California, Berkeley, California 94720-1740, USA*
[2]*Department of Engineering Sciences and Applied Mathematics, Northwestern University, Evanston, Illinois 60208, USA*

(Received 18 January 2006; published 24 May 2006)

An experimental investigation of explosive crystallization (EC) of thin amorphous Ge films deposited on a solid substrate is performed, and a theory of EC front propagation accompanied by melting in a class of films that includes Ge films is developed. The experiments show that the propagation of a planar EC front is possible for a certain range of substrate temperatures and film thicknesses. It is found that for substrate temperatures larger than a certain threshold, the macroscopically planar front leaves behind a columnar microstructure in the crystal. The theory of EC front propagation is based on the experimental observation that the propagating front exhibits a thin layer of Ge melt between the amorphous and crystalline phases. A uniformly propagating planar front solution is determined, whose propagation speed is found as a function of the substrate temperature and the heat loss parameter that, in turn, depends on the film thickness. A linear stability analysis of the uniformly propagating EC front with a melting layer is performed. It is found that in a certain interval of substrate temperatures the EC front undergoes a monotonic morphological instability with a preferred wave number that explains the formation of the columnar structures observed in experiments. We also perform a nonlinear analysis describing the evolution of the morphological instability. The interval of substrate temperatures for which the instability is observed, as well as the wavelength of the columnar structure, are found to be in good agreement with experimental observations.

DOI: 10.1103/PhysRevB.73.184125 PACS number(s): 81.05.Cy, 81.10.Fq, 66.10.Cb, 68.18.Jk

I. INTRODUCTION

Laser processing of thin amorphous semiconductor films of Si and Ge deposited on insulator substrates (glass, quartz, etc.) is important for fabricating, e.g., solar cells, flat panel displays, and infrared detectors. This process has recently received renewed attention.[1–4] During the processing, an amorphous film (formed on the substrate by rapid vapor cooling) is transformed into a crystalline film. One of the principal mechanisms of this transformation is explosive crystallization (EC)[5] which usually occurs as a self-propagating front of phase transformation from an amorphous to a crystalline phase driven by the large heat release accompanying the phase transition. A better understanding of underlying physics of explosive crystallization may enable efficient creation of ultralarge crystalline films deposited on the insulating substrates and improvements in crystal quality. Geiler has classified four types of explosive crystallization: explosive solid-phase nucleation, explosive solid-phase epitaxy, explosive liquid-phase nucleation, and explosive liquid-phase epitaxy (ELPE).[6] Two of these types are characterized by a liquid zone that mediates the phase change phenomenon. One of these types, specifically ELPE, is of particular interest here. When the front in a thin film exhibits a narrow melt zone between the amorphous and crystalline phases, extremely large crystallization velocities and crystallization distances can be achieved. This regime is typical of materials with large differences between the crystalline and amorphous melting temperatures and enthalpies. During explosive crystallization of such materials, the heat released due to crystallization of the melt induces melting of the adjacent amorphous phase. This leads to the self-sustained propagation of the *two* phase transition fronts, the melt-crystal and amorphous-melt fronts (see Fig. 1), moving with the same speed with a constant distance between them. That is, propagation is driven by the heat released in crystallization which diffuses into the melt and amorphous regions, raising their temperature to a value sufficiently high to melt the adjacent amorphous layer. Crystallization of the undercooled melt is again initiated and the process repeats. This process can continue over very large distances.

Typical frontal propagation speeds are about 10 m/s. The thickness of the mediating liquid layer estimated by atomistic computer simulations ranges from 27 to 117 Å, depend-

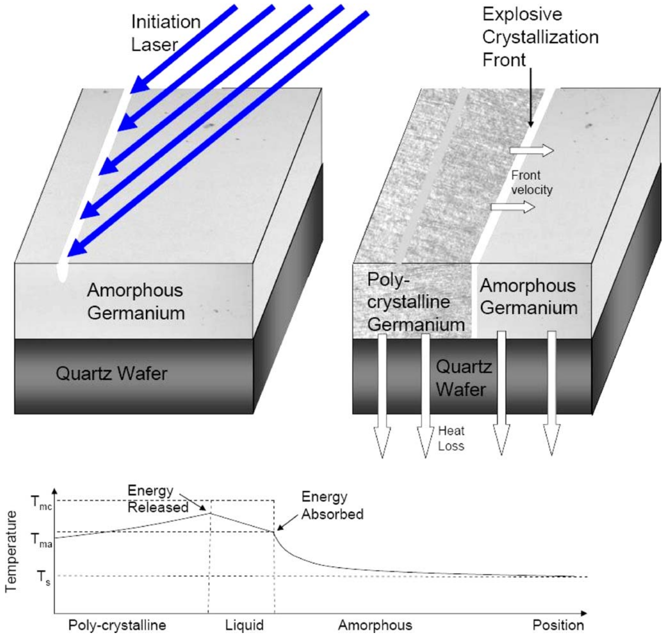

FIG. 1. (Color online) Schematic representation of explosive crystallization in the ELPE mode.

1098-0121/2006/73(18)/184125(15)

ing on heat loss.[9] Experimental electrical conductivity calculations on 3 micron thick germanium film estimate the liquid layer to be less than 10 nm thick.[7] The self-sustaining nature of explosive crystallization is dependent upon heat conduction losses to the substrate. Explosive crystallization will continue as long as the latent heat released upon crystallization exceeds the heat losses from the sample, by an amount sufficient to melt the adjacent amorphous solid. The two competing factors, heat release and heat loss, result in variable crystal growth characteristics that can yield different crystal morphologies. Investigation of the effects of heat loss during explosive crystallization revealed three distinct morphological regimes.[7,8] High heat losses and relatively low propagation speeds resulted in a so-called scalloped structure, in which the resulting crystalline film exhibits a striped structure with the stripes parallel to the front, i.e., normal to the front propagation direction. Such a structure is most likely produced by an oscillatory instability of the propagating explosive crystallization front that leads to oscillations of the frontal speed.[10,11] Another regime, characterized by low heat losses and frontal speeds relatively independent of temperature, produced a so-called "columnar structure" which is a striped structure with stripes normal to the front, i.e., parallel to the front propagation direction. Such a structure can arise due to a cellular morphological (Mullins-Sekerka) instability of the crystallization front.[11,12] Last, a mixed or transitional morphology was observed between these two regimes.

Since the melt layer propagating through an amorphous film in ELPE explosive crystallization is so thin, it is difficult to directly characterize the shape and growth characteristics of the two traveling interfaces. In this paper we present a combined experimental and theoretical investigation of explosive crystallization of Ge films in the ELPE mode. We perform experiments on samples of Ge films of different thickness and observe planar EC fronts propagating over long distances through the samples, leaving behind crystalline structures which are either spatially uniform or have one of a number of morphologies (scalloped, columnar, or transitional). Our theoretical computations of the frontal speed of the uniformly propagating planar front as a function of the substrate temperature and the film thickness show good agreement with the experimental observations. In addition, we perform a linear stability analysis of the propagating planar EC front and show that the columnar structure can be explained by the cellular instability of the front, which is similar to the Mullins-Sekerka instability. Finally, we also perform a nonlinear analysis describing the evolution of the morphological instability.

In Sec. II we describe the experimental setup and in Sec. III the experimental results. In Sec. IV we present the mathematical model of EC front propagation. A uniformly propagating front solution of the model is presented in Sec. V and its linear stability is considered in Sec. VI. In Sec. VII we describe the nonlinear evolution of the morphological instability. Finally, a summary appears in Sec. VIII.

II. EXPERIMENTAL SETUP

Amorphous germanium was deposited on quartz wafers via sputtering. Two types of samples were prepared, with the film thickness of 0.89 and 1.8 microns. The thickness was verified by Rutherford backscattering. The deposition rate was 44.5 nm/min and 36.0 nm/min, respectively. The wafers were cleaved using a dicing saw, creating square samples with a side length of a half a centimeter. After creation, these samples were investigated using an atomic force microscope (AFM). The RMS roughness was determined to be less then 3.8 and 2.3 nm for the 0.89 and 1.8 micron samples, respectively.

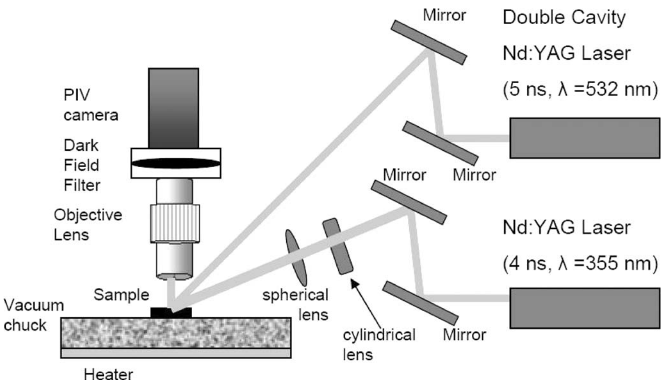

FIG. 2. Experimental setup used to induce and record in situ images of explosive crystallization. The spherical lens has a focal length of 100 mm and the cylindrical lens has a focal length of 80 mm. 10×, 20×, and 50× objective lenses were used.

Figure 2 schematically displays the complete experimental arrangement used to induce and record in situ images of explosive crystallization in germanium. A heater capable of a maximum temperature of 873 K controls the heat loss to the substrate. A higher temperature corresponds to a lower heat loss, which may result in columnar crystal growth. A frequency tripled Nd:YAG laser ($t_{\text{pulse}}=4$ ns, $\lambda=355$ nm) was focused to a line using a cylindrical lens of focal length 80 mm and a spherical lens of focal length 100 mm. Approximately 151 μJ was supplied in the initiation pulse of roughly 5 mm by 35 microns in dimension. The pulse was incident at 45° to the sample. A frequency doubled, double-cavity Nd:YAG laser ($t_{\text{pulse}}=5$ ns, $\lambda=532$ nm) was used as an illumination source. Also incident at 45° to the sample, this laser provided two off-axis illumination flashes separated by varying times. The images were captured using a 12 bit CCD by Sensicam. Two 1280×1024 black and white images could be captured with as short a separation as 200 ns. Two four-channel Stanford Research Systems Delay Generator 535 and an eight-channel BNC 555 Digital Delay/Pulse Generator were used to precisely control the timing of the setup. A photo detector and 500 MHz HP Infinium Oscilloscope were used to detect and record a reflected portion of the Nd:YAG 355 nm initiation pulse and both Nd:YAG 532 nm illumination pulses. The velocity of the crystallization front is calculated from the distance traveled between pictures and the known time between Nd:YAG illumination pulses. A dark field filter was used to capture the higher order reflections for in situ images. Orientation of the illumination laser relative to the crystal growth direction is paramount for clear images of the 0.89 micron sample. AFM scans of the 0.89 micron sample after crystallization reveal grain heights of only a few nanometers, with the exception of grain colli-

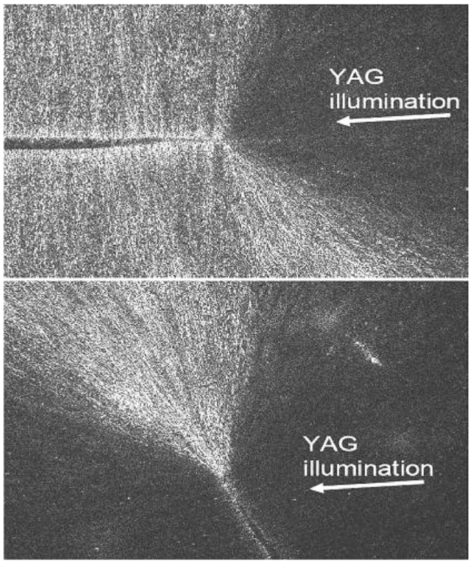

FIG. 3. Crystal grain resolution depends upon illumination orientation relative to crystal growth. A completely crystallized 0.89 micron sample is illuminated from the right in both images. The bottom image differs from the top image by approximately 120°.

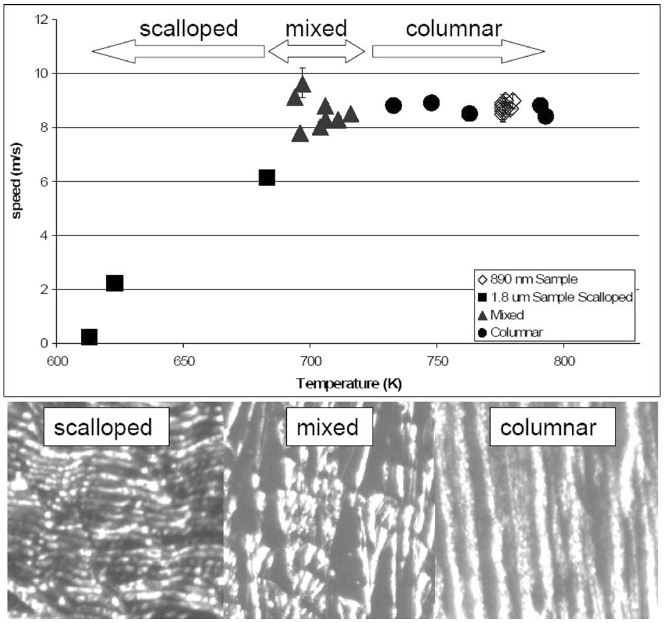

FIG. 4. Explosive crystallization velocity as a function of substrate temperature. Micrographs 40 microns in width are shown of the scalloped, mixed, and columnar regimes explosively crystallized on the 1.8 micron sample.

sions resulting in 30 nm high ridges. This small increase in surface roughness coupled with a reflectivity change of less than 10%[13] was not sufficient for imaging purposes, but the diffraction caused by the grains provides a clear image (see Fig. 3). Figure 3 shows two dark field images of a crystallized sample, with the bottom image rotated counterclockwise by approximately 120°. The entire sample is crystallized; however, only the grains oriented orthogonally to the incoming Nd:YAG laser illumination pulse diffract light sufficiently for imaging with the Sensicam CCD camera. This effect was less critical for the 1.8 micron sample which was much rougher after crystallization. AFM scans of the 1.8 micron sample revealed grain heights to be around 100 nm with up to 300 nm ridges caused by grain collisions.

Initial tests were run to determine a range of temperatures in which explosive crystallization would occur for this film preparation and thickness. The sample was placed on the heater for times ranging from 1 s to 5 min prior to initiation. This range was tested to evaluate the time at which appreciable solid phase crystallization occurred. Setting a heater temperature and delaying the start time of the experiment until explosive crystallization was inhibited revealed information on this time. The 0.89 micron sample was found to no longer explosively crystallize in slightly under 30 s at 773 K. The 1.8 micron sample remained unaffected at times up to 5 min. Initiation was induced approximately 15 s after placement on the heater for the 0.89 micron sample, and 30 s for the 1.8 micron sample to ensure that thermal equilibrium was reached while minimizing solid phase crystallization.

III. EXPERIMENTAL RESULTS

Dozens of samples were tested at various temperatures. The time separation between pictures was varied between 1 and 40 ms. Velocity calculations were performed on the longer delay times to minimize uncertainty errors. Three regimes, characterized by three different morphologies of the crystalline film resulting from EC were observed. The columnar growth regime revealed a stable 8.75±0.15 m/s crystallization speed. The scalloped and transitional regimes showed a temperature-dependent crystallization velocity, as seen in Fig. 4. No difference was found in the speed of propagation between the 1.8 micron and 0.89 micron samples; however, the range of temperatures at which crystallization could be induced was found to vary drastically. Explosive crystallization was observed between 753 and 803 K for the 0.89 micron sample. The columnar regime was the only one observed. The 1.8 micron sample explosively crystallized at a temperature between 613 and 803 K. EC at lower temperatures exhibited the transitional and scalloped regimes. The ability of the 1.8 micron sample to explosively crystallize at lower temperatures is due to the increase in latent heat released from the thicker film during crystallization of the melt. The dependence of the front velocity on temperature is very similar to that found in Ref. 8. The transition temperature between the scalloped and transitional, and transitional and columnar growth regions are approximately 50 K above that found in Ref. 8. This discrepancy can be explained by the difference in heat loss parameters. The silicon wafer used in Ref. 8 leads to a higher heat loss parameter than for our quartz substrate. Hence at any given temperature the heat loss is lower in our experiments, effectively shifting the curve to higher temperatures. The calculated speed is slightly slower in our experiments. The frontal speeds reported in Ref. 8 for low heat losses are generally around 12 m/s. This may be due to a difference in film preparation.

Experiments carried out in the columnar regime revealed repeatable and predictable results. As can be seen in Fig. 4,

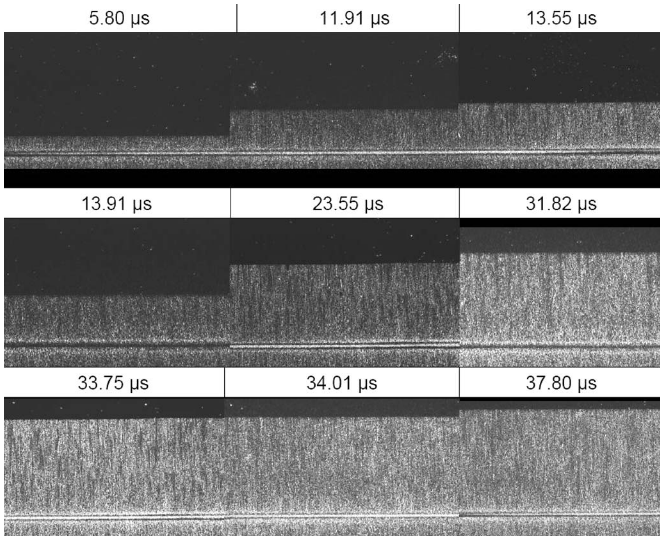

FIG. 5. A series of dark field *in situ* images taken on the 0.89 μm germanium sample. Time after the initiation pulse is shown at the top of each picture. The horizontal line toward the bottom of each picture was caused by the initiation pulse. The white region is the growing crystal, and the black is amorphous germanium. Each picture is 650 microns $\times$ 520 microns (length $\times$ height).

the speed of propagation was almost constant. Figure 5 shows that the front propagation is very stable. Figure 5 was created from five different experiments done by explosively crystallizing the 0.89 micron sample with a substrate temperature of 776 K. The time of the picture acquisition with respect to the initiation pulse is shown at the top of each picture. The horizontal initiation line can be seen toward the bottom of each picture. At early times (upper left of figure) the crystallization front has not traveled far. The black toward the top of the photo is amorphous germanium, still unaffected by the explosive crystallization. The linearity of the crystallization front remains throughout the entire field of view, a crystal growth of 425 microns in length. Use of a 10$\times$ objective lens allowed the front to be viewed in situ at a distance of up to 936 microns. Even over this substantial crystal length the front remained very linear. Use of a 50$\times$ objective lens gives resolution of 0.5 microns. At these high resolutions the front appeared linear. Though Fig. 5 is shown for the 0.89 micron sample, the results for the 1.8 micron sample were very similar.

Although substrate temperature variations did not affect crystal growth velocity in the columnar regime, there was an observable effect on the average width of the resulting crystal "columns," i.e., the average wavelength of the columnar structure. It decreased with temperature as can be seen in Table I. The average columnar structure wavelength was measured after the crystal "columns" had grown to approximately 100 microns in length. We note also that the average width of the "columns" (the columnar structure wavelength) in the beginning of the front propagation, in close proximity to the initiation site, was smaller but was very difficult to quantify. A steady state width was reached after the front propagated approximately 50 microns.

TABLE I. The average wavelength of the columnar structure as a function of the substrate temperature.

T_s K	μm/peak
740	6.0
751	5.9
768	4.8
770	5.2

Investigation of the transitional and scalloped regime gives very different results for the explosive crystallization interface shape. These regimes are plagued by collisions between grains growing in different directions. The same line melt which initiated a uniform crystallization front at higher temperatures ceases to do so at lower temperatures. Increasing the laser energy to compensate for the lower substrate temperature does not solve the problem. Discrete initiation points are formed in the transitional regime. These initiation points become sparser as the temperature drops and eventually disappear altogether below 613 K for the 1.8 micron sample. This can be seen in the in situ dark field images in Fig. 6. These images are especially informative as other techniques would not detect a nonuniform initiation. Although crystallization was initiated at discrete points, the entire sample crystallizes as the heat loss is not sufficiently large to quench the traveling phase change.

Figure 7 shows the effects of multiple initiation sites on the front shape. This figure is an *in situ* image taken 50 μs after the initiation pulse. Massive collisions between growing grains result in large raised bumps. AFM scans revealed these bumps to be up to 300 nm. The crystal collisions occur due to the lack of uniformity in initiation. This is revealed in the first image (upper left) of Fig. 6, which displays the same crystal growth as Fig. 7 at 6 μs after initiation. Figure 8 is an image collected on a sample which has completely crystallized in the transitional regime. This picture shows the individual grain boundaries and their termination due to collisions with grains growing in a different direction.

The scalloped regime occurred at the lowest substrate temperatures where explosive crystallization was observed. Figure 9 shows the distinct topography of a sample crystallized in this regime. Very few initiation locations were observed and crystallization proceeded radially away from these locations. Collisions were evident in this regime as

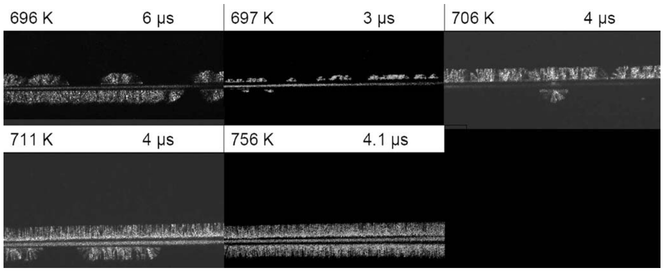

FIG. 6. In the transitional regime, an increase in temperature causes an increase in initiation points. Eventually a uniform initiation line is created (756 K). The time of the image after initiation is shown in the upper right of each frame. Each frame is 520 microns in length.

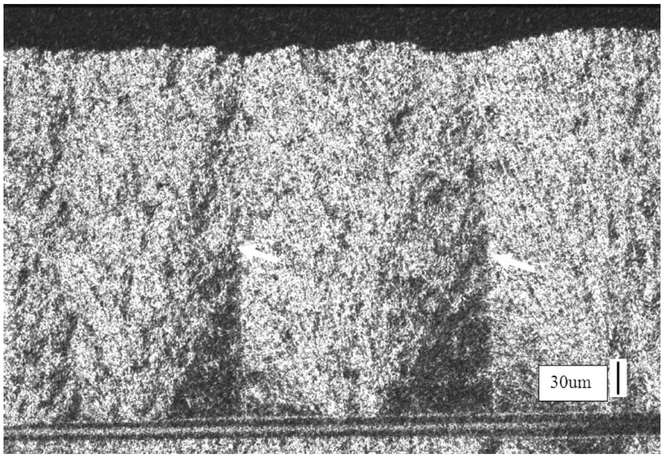

FIG. 7. This dark field image taken 50 μs after initiation with a substrate temperature of 696 K shows clear crystal grain collisions. The horizontal line at the bottom of the image is the initiation melt. The macroscopic crystal growth direction is toward the top of the image. Major collisions of horizontally growing grains can be seen leading to the two vertical lines highlighted by the arrows.

well. The macroscopic crystal growth direction differed from the microscopic crystal growth direction due to these collisions. In the next section we present a theory of EC in the presence of melting that will allow us to explain certain experimental observations described above.

IV. MATHEMATICAL MODEL

Consider explosive crystallization of a thin, amorphous film deposited on a solid substrate. We assume that EC occurs via a two-stage process in which the amorphous material first melts and then solidifies into a crystalline phase. This process leads to the propagation of an EC front that consists of a thin layer of melt separating the amorphous and crystalline phases. The melt temperature is lower than the equilibrium melting temperature of the crystalline phase but is higher than the equilibrium melting temperature of the amorphous phase, so that the melt is undercooled with respect to the crystalline phase and overheated with respect to the amorphous phase. In this configuration, after initiation the heat released due to crystallization of the undercooled melt diffuses towards the amorphous phase and raises its temperature to a value sufficiently high to melt it. Crystallization of the resulting undercooled melt is again initiated and the process repeats. This leads to self-propagation of the front through the film. EC front propagation is governed by the processes of heat transfer through the amorphous, liquid, and crystalline phases, melting of the amorphous phase, and solidification of the melt to form the crystalline phase. The propagation velocity depends on the interfacial temperatures (interface response functions).

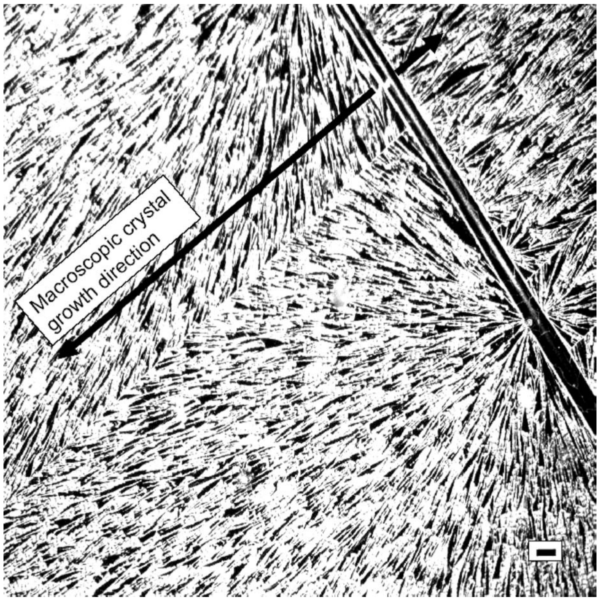

FIG. 8. Another example of crystal grain collisions is shown in this dark field image. This image was taken after explosive crystallization of the entire substrate was completed for a sample in the transitional regime. The scale bar is 35 microns.

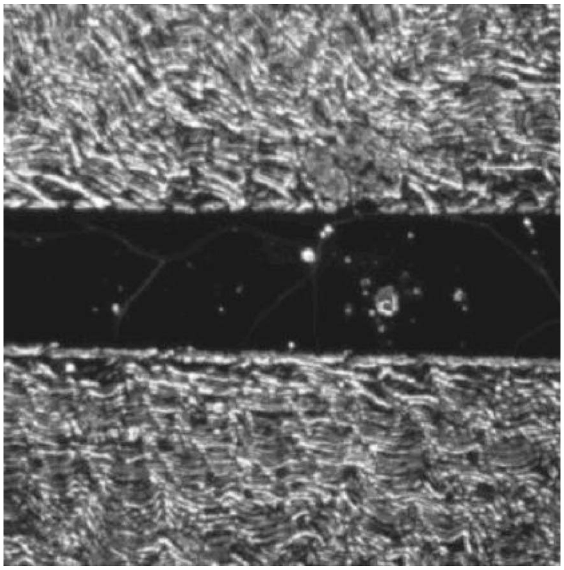

FIG. 9. A dark field image of a 1.8 micron sample crystallized sample in the scalloped regime. The width of the melt line is 35 microns.

Since the film is thin, temperature variations across film can be neglected, and EC in the film can be described by a two-dimensional model with the z coordinate along the direction of planar front propagation (normal to the planar front) and the x coordinate along the planar front. The governing equations and boundary conditions for the temperature field $T(z,x,t)$ and the shapes of the crystal-melt and melt-amorphous interfaces $\zeta_1(x,t)$ and $\zeta_2(x,t)$, respectively, are

$$\rho c_f \frac{\partial T}{\partial t} = \lambda_c \nabla^2 T - \gamma(T - T_s), \quad z < \zeta_1(x,t), \tag{1}$$

$$\rho c_f \frac{\partial T}{\partial t} = \lambda_m \nabla^2 T - \gamma(T - T_s), \quad \zeta_1(x,t) < z < \zeta_2(x,t), \tag{2}$$

$$\rho c_f \frac{\partial T}{\partial t} = \lambda_a \nabla^2 T - \gamma (T - T_s), \quad z > \zeta_2(x,t), \tag{3}$$

$$z = \zeta_1(x,t):\ T_c = T_m, \tag{4}$$

$$v_n^{\mathrm{mc}} L_{\mathrm{mc}} = \mathbf{n}_1 \cdot (\lambda_c \nabla T_c - \lambda_m \nabla T_m), \tag{5}$$

$$z = \zeta_2(x,t):\ T_m = T_a, \tag{6}$$

$$-v_n^{\mathrm{ma}} L_{\mathrm{ma}} = \mathbf{n}_2 \cdot (\lambda_m \nabla T_m - \lambda_a \nabla T_a), \tag{7}$$

$$z \to \pm\infty:\ T \to T_s, \tag{8}$$

where T_c, T_m, and T_a are the temperatures in the crystalline, melt, and amorphous phases corresponding to $z < \zeta_1$, $\zeta_1 < z < \zeta_2$, and $z > \zeta_2$, respectively, T_s is the substrate temperature $\mathbf{n}_{1,2} = (-\partial_x \zeta_{1,2}, 1)/\sqrt{1 + (\partial_x \zeta_{1,2})^2}$ are the normal vectors at the respective interfaces, λ is the thermal conductivity, L_{ma} and L_{mc} are the latent heats of melting per unit volume of the amorphous and crystalline phases, respectively, ρ, c_f, and γ are the density, specific heat, and the heat-loss parameter, each assumed to be the same constant in all three phases. The boundary conditions (4) and (6) describe the continuity of the temperature distribution at the melt-crystal and melt-amorphous interfaces, while the boundary conditions (5) and (7) describe the heat flux balances at the moving interfaces. The normal velocities of the melt-crystal and melt-amorphous interfaces

$$v_n^{\mathrm{mc}} = \frac{\partial_t \zeta_1}{\sqrt{1 + (\partial_x \zeta_1)^2}}, \quad v_n^{\mathrm{ma}} = \frac{\partial_t \zeta_2}{\sqrt{1 + (\partial_x \zeta_2)^2}}, \tag{9}$$

depend on the interfacial temperatures T_{ci} and T_{ai} according to the Frenkel-Wilson kinetic law[6,9,14] that describes the motion of a nonequilibrium phase boundary as the result of thermally activated jumps of atoms with the activation barrier proportional to the difference in the free energies of the two phases

$$v_n^{\mathrm{mc}} = F_c(T_{ci}) \equiv A_{\mathrm{mc}} \exp\left[-\frac{E_{\mathrm{mc}}}{k_B T_{ci}}\right] \times \left\{1 - \exp\left[\frac{L_{\mathrm{mc}}}{k_B N_m}\left(\frac{1}{T_{\mathrm{mc}}} - \frac{1}{T_{ci}}\right)\right]\right\}, \tag{10}$$

$$v_n^{\mathrm{ma}} = F_a(T_{ai}) \equiv A_{\mathrm{ma}} \exp\left[-\frac{E_{\mathrm{ma}}}{k_B T_{ai}}\right] \times \left\{\exp\left[\frac{L_{\mathrm{ma}}}{k_B N_a}\left(\frac{1}{T_{\mathrm{ma}}} - \frac{1}{T_{ai}}\right)\right] - 1\right\}. \tag{11}$$

Here $F_c(T_{ci})$ and $F_a(T_{ai})$ are the so-called interfacial response functions in which the constants A_{mc} and A_{ma} are pre-exponential factors, E_{mc} and E_{ma} are activation energies, $N_{m,a}$ are the number densities of the respective phases, k_B is the Boltzmann constant, and T_{mc} and T_{ma} are the equilibrium melting temperatures of the crystalline and amorphous materials, respectively, that depend on the curvature of the interface according to the Gibbs-Thomson relation

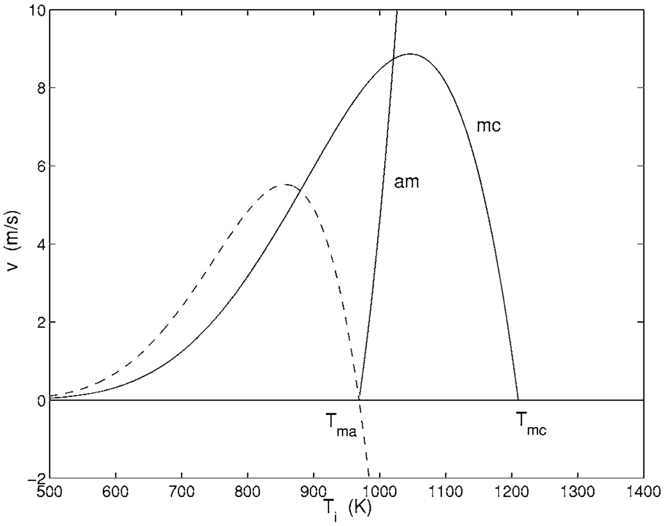

FIG. 10. Solid lines: interface response functions $F_c(T_i)$ and $F_a(T_i)$ defined by Eqs. (10) and (11) that determine the dependence of the interface speed on the interfacial temperature T_i for germanium: mc: speed of Ge melt crystallization front; am: speed of amorphous Ge melting front. Dashed line: speed of Ge melt solidification into amorphous phase. The parameters are $E_{\mathrm{mc}} = 0.5$ eV $= 8.0 \times 10^{-20}$ J, $E_{\mathrm{ma}} = 0.52$ eV $= 8.32 \times 10^{-20}$ J, $A_{\mathrm{mc}} = 0.53 \times 10^4$ m/s, $A_{\mathrm{ma}} = 1.9 \times 10^4$ m/s, $L_{\mathrm{mc}} = 2.703 \times 10^9$ J m^{-3}, $L_{\mathrm{ma}} = 1.7 \times 10^9$ J m^{-3}, $T_{\mathrm{mc}} = 1210$ K, $T_{\mathrm{ma}} = 969$ K, $N_a = 4.15 \times 10^{28}$, $N_m = 4.56 \times 10^{28}$.

$$T_{\mathrm{mc}} = T_{\mathrm{mc}}^0[1 - d_{\mathrm{mc}} K_1], \quad T_{\mathrm{ma}} = T_{\mathrm{ma}}^0[1 - d_{\mathrm{ma}} K_2], \tag{12}$$

where T_{mc}^0 and T_{ma}^0 are the equilibrium melting temperatures at the planar interfaces

$$d_{\mathrm{mc}} = \frac{\sigma_{\mathrm{mc}}}{L_{\mathrm{mc}}}, \quad d_{\mathrm{ma}} = \frac{\sigma_{\mathrm{ma}}}{L_{\mathrm{ma}}}$$

are the respective capillary lengths, with σ_{mc} and σ_{ma} being the respective surface energies, and K_1, K_2 are the interfacial curvatures

$$K_{1,2} = -\frac{\partial^2 \zeta_{1,2}/\partial x^2}{[1 + (\partial \zeta_{1,2}/\partial x)^2]^{3/2}}.$$

Typical plots of the interfacial response functions $F_c(T_i)$ and $F_a(T_i)$ are shown in Fig. 10 by the solid lines. The curve "mc" corresponds to $F_c(T_i)$ and the line "am" corresponds to $F_a(T_i)$. Note that the line "am" (the so-called "melting branch″) is the reflection of the negative part of the curve shown by the dashed line which corresponds to the solidification of the melt into the amorphous phase and is similar to the "mc" curve for the undercooled melt crystallization. The mathematical model formulated above is similar to the one considered in Ref. 6 for EC of a thin film of silicon in ELPE mode.

We choose $v_0 = A_{\mathrm{mc}} \exp[-E_{\mathrm{mc}}/k_B T_s]$ as the velocity scale, $l_0 = \lambda_c/(\rho c_f v_0)$ as the length scale, and $t_0 = l_0/v_0$ as the time scale, and introduce the dimensionless temperature, $\theta = (T - T_s)/T^*$, where $T^* = L_{\mathrm{mc}}/(\rho c_f)$. Then, in dimensionless form the system (1)–(11) reads

$$\frac{\partial\theta_c}{\partial t} = \nabla^2\theta_c - \alpha\theta_c, \quad z < \zeta_1(x,t) \tag{13}$$

$$\frac{\partial\theta_m}{\partial t} = \chi_m\nabla^2\theta_m - \alpha\theta_m, \quad \zeta_1(x,t) < z < \zeta_2(x,t), \tag{14}$$

$$\frac{\partial\theta_a}{\partial t} = \chi_a\nabla^2\theta_a - \alpha\theta_a, \quad z > \zeta_2(x,t), \tag{15}$$

$$z = \zeta_1(x,t)\colon\ \theta_c = \theta_m, \tag{16}$$

$$\frac{\partial_t\zeta_1}{\sqrt{1+(\partial_x\zeta_1)^2}} = f_c(\theta) = \mathbf{n}_1(\boldsymbol{\nabla}\theta_c - \chi_m\boldsymbol{\nabla}\theta_m), \tag{17}$$

$$z = \zeta_2(x,t)\colon\ \theta_m = \theta_a, \tag{18}$$

$$-q\frac{\partial_t\zeta_2}{\sqrt{1+(\partial_x\zeta_2)^2}} = -qf_a(\theta) = \mathbf{n}_2(\chi_m\boldsymbol{\nabla}\theta_m - \chi_a\boldsymbol{\nabla}\theta_a), \tag{19}$$

$$z \to \pm\infty\colon\ \theta \to 0, \tag{20}$$

where $\alpha=\gamma\lambda_c/(\rho c_f v_0^2)$ is the dimensionless heat-loss parameter, $\chi_{m,a}=\lambda_{m,a}/\lambda_c$, $q=L_{\mathrm{ma}}/L_{\mathrm{mc}}$, and for simplicity, the dimensionless space and time coordinates have the same notation as the dimensional coordinates. The dimensionless interface response functions are

$$f_c(\theta) = \exp\left[e_c\frac{\beta\theta}{1+\beta\theta}\right] \times \left\{1-\exp\left[\epsilon_c\left(\frac{1}{1-\delta_c k_1} - \frac{\tau_c}{1+\beta\theta}\right)\right]\right\}, \tag{21}$$

$$f_a(\theta) = w\exp\left[e_a\frac{\beta\theta}{1+\beta\theta}\right] \times \left\{\exp\left[\epsilon_a\left(\frac{1}{1-\delta_a k_2} - \frac{\tau_a}{1+\beta\theta}\right)\right] - 1\right\}, \tag{22}$$

where

$$\beta = \frac{T^*}{T_s}, \quad \tau_c = \frac{T_{\mathrm{mc}}}{T_s}, \quad \tau_a = \frac{T_{\mathrm{ma}}}{T_s}, \quad e_c = \frac{E_{\mathrm{mc}}}{k_BT_s}, \quad e_a = \frac{E_{\mathrm{ma}}}{k_BT_s},$$

$$\epsilon_c = \frac{L_{\mathrm{mc}}}{k_BN_mT_{\mathrm{mc}}}, \quad \epsilon_a = \frac{L_{\mathrm{ma}}}{k_BN_aT_{\mathrm{ma}}},$$

$$w = \frac{A_{\mathrm{ma}}}{A_{\mathrm{mc}}}\exp\left[\frac{E_{\mathrm{mc}}-E_{\mathrm{ma}}}{k_BT_s}\right],$$

$$\delta_c = d_{\mathrm{mc}}/l_0, \quad \delta_a = d_{\mathrm{ma}}/l_0, \quad (k_1,k_2) = (K_1,K_2)l_0.$$

V. UNIFORMLY PROPAGATING EC FRONT

We seek a solution of the system (13)–(22) in the form of a uniformly propagating EC front that consists of planar, crystal-melt, and melt-amorphous interfaces, moving with the same speed V and separated by a distance l,

$$\theta_{c,m,a} = \theta^{(0)}_{c,m,a}(z-Vt), \quad \zeta_1 = Vt, \quad \zeta_2 = l+Vt. \tag{23}$$

We substitute Eq. (23) into Eqs. (13)–(22) to obtain

$$\theta^{(0)}_c = A_0e^{\xi r_+},$$

$$r_+ = \frac{1}{2}[-V+\sqrt{V^2+4\alpha}], \quad \xi < 0, \tag{24}$$

$$\theta^{(0)}_m = B_0e^{\xi s_+} + C_0e^{\xi s_-},$$

$$s_\pm = \frac{1}{2\chi_m}[-V\pm\sqrt{V^2+4\alpha\chi_m}], \quad 0<\xi<l, \tag{25}$$

$$\theta^{(0)}_a = D_0e^{\xi p_-},$$

$$p_- = \frac{1}{2\chi_a}[-V+\sqrt{V^2+4\alpha\chi_a}], \quad \xi > l, \tag{26}$$

where $\xi=z-Vt$, and

$$A_0 = \frac{V}{\Delta_0}[e^{ls_-}(\chi_ap_- - \chi_ms_-) + e^{ls_+}(\chi_ms_+ - \chi_ap_-) - \chi_mq(s_+ - s_-)],$$

$$B_0 = \frac{V}{\Delta_0}[e^{ls_-}(\chi_ap_- - \chi_ms_-) + q(\chi_ms_- - r_+)],$$

$$C_0 = -\frac{V}{\Delta_0}[e^{ls_+}(\chi_ap_- - \chi_ms_+) + q(\chi_ms_+ - r_+)],$$

$$D_0 = \frac{V}{\Delta_0}e^{-lp_-}[e^{ls_+}q(\chi_ms_- - r_+) + \chi_me^{l(s_++s_-)} - e^{ls_-}q(\chi_ms_+ - r_+)],$$

$$\Delta_0 = e^{ls_-}(r_+ - \chi_ms_+)(\chi_ap_- - \chi_ms_-) - e^{ls_+}(r_+ - \chi_ms_-)(\chi_ap_- - \chi_ms_+). \tag{27}$$

In the special case when the thermal conductivities of all three phases are equal $(\chi_a=\chi_m=1)$, these expressions simplify to

$$A^e_0 = \frac{V}{\Gamma_0}(1-qe^{-lr_+}), \quad B^e_0 = -\frac{V}{\Gamma_0}qe^{-lr_+}, \quad C^e_0 = \frac{V}{\Gamma_0},$$

$$D^e_0 = \frac{V}{\Gamma_0}(1-qe^{-lr_-}), \quad \Gamma_0 = \sqrt{V^2+4\alpha},$$

$$r_\pm = (-V\pm\Gamma_0)/2, \quad s_\pm = r_\pm, \quad p_- = r_-. \tag{28}$$

We will consider this special case in the stability analysis in the next section.

The velocity of the two interfaces V and the distance between them l are found from the solution of the following system of nonlinear transcendental equations:

$$V = f_c[\theta_c^{(0)}(0)] = f_a[\theta_a^{(0)}(l)], \tag{29}$$

where $\theta_c^{(0)}$ and $\theta_a^{(l)}$ are defined in Eqs. (24)–(27) and the interfacial response functions $f_{a,c}(\theta)$ are defined in Eqs. (21) and (22).

Thus, the velocity of a uniformly propagating EC front and the thickness of the melt layer are complicated functions of the substrate temperature, the heat-loss coefficient, the latent heats of melting of the amorphous and crystalline phases, the kinetic parameters of the interface response functions, as well as the thermophysical parameters. i.e., the thermal conductivities and specific heat. In experiments, when a particular material is used, the most common control parameters are the substrate temperature T_s and the film thickness h that determines the heat-loss parameter γ. The latter can be estimated in the following way. The heat flux from the film into the substrate is $j=\lambda_s(T-T_s)/\delta_s$, where T is the film temperature, λ_s is the substrate thermal conductivity, and δ_s is the thickness of the thermal boundary layer in the substrate, near the film-substrate interface. For δ_s one obtains $\delta_s \sim \sqrt{\kappa_s \tau}$, where κ_s is the substrate thermal diffusivity and τ is the characteristic time of heat transfer. For a front moving with the speed v, one can estimate $\tau \sim \delta_f/v$, where δ_f is the thickness of the thermal boundary layer in the film near the moving front. For δ_f one obtains $\delta_f \sim \kappa_f/v$, where κ_f is the thermal diffusivity of the film. Thus, one obtains for the heat flux into the substrate $j=\frac{\lambda_s v}{\sqrt{\kappa_s \kappa_f}}(T-T_s)$. Under the assumption that the temperature is constant across the thin film with thickness h, the differential heat balance for a piece of film having contact area $dA=dxdz$ with the substrate, yields $\rho_f c_f h dA(\partial T/\partial t)=\lambda_f[(\partial T/\partial z)_{z+dz}-(\partial T/\partial z)_z]hdx + \lambda_f[(\partial T/\partial x)_{x+dx}-(\partial T/\partial x)_x]hdz - jdA$. Therefore, for the heat-loss parameter in Eqs. (1)–(3) one obtains

$$\gamma = \frac{\lambda_s}{\delta_s \rho_f c_f h} = \sqrt{\frac{\kappa_s}{\kappa_f}} \frac{\rho_s c_s}{\rho_f c_f} \frac{v}{h}. \tag{30}$$

One can see that the heat-loss parameter is inversely proportional to the film thickness: the thinner the film the greater the heat losses.

We have computed the characteristics of steady-state propagation of a planar EC front, using parameter values corresponding to a film of amorphous germanium: $L_{\mathrm{ma}}=1.7\times10^9$ J m^{-3}, $L_{\mathrm{mc}}=2.703\times10^9$ J m^{-3}, $T_{\mathrm{ma}}=969$ K, $T_{\mathrm{mc}}=1210$ K, $\lambda_a=25.15$ W m^{-1} K^{-1}, $\lambda_m=49.43$ W m^{-1} K^{-1}, $\lambda_c=17.40$ W m^{-1} K^{-1}, $\kappa_a=6.32\times10^{-6}$ m^2 s^{-1}, $\kappa_m=2.36\times10^{-5}$ m^2 s^{-1}, $\kappa_c=8.28\times10^{-6}$ m^2 s^{-1}, $\rho_f c_f=2.73\times10^6$ J m^{-3} K^{-1}, $\rho_s c_s=2.31\times10^6$ J m^{-3} K^{-1}, $E_{\mathrm{ma}}=0.52$ eV $=8.32\times10^{-20}$ J, $E_{\mathrm{mc}}=0.5$ eV$=8.0\times10^{-20}$ J, $A_{\mathrm{mc}}=0.53\times10^4$ m/s, $A_{\mathrm{ma}}=1.9\times10^4$ m/s, $N_a=4.15\times10^{28}$, $N_m=4.56\times10^{28}$. Since the precise values of the kinetic parameters for the interfacial response functions: the pre-exponential factors A_{ma} and A_{mc}, and the activation energies E_{ma} and E_{mc} for germanium could not be found in the experimental literature, we have taken them of the correct order of magnitude and such that they yield the average (over various values of T_s) of the EC front propagation speeds observed in our experiments. The heat-loss parameter γ was estimated using Eq. (30), taking $v=8.75$ m/s which was observed in the experiments described above. For example, for a 1.8-micron-thick germanium film ($h=1.8\times10^{-6}$ m) on a quartz substrate, we estimate $\gamma=1.06\times10^6$ s^{-1}.

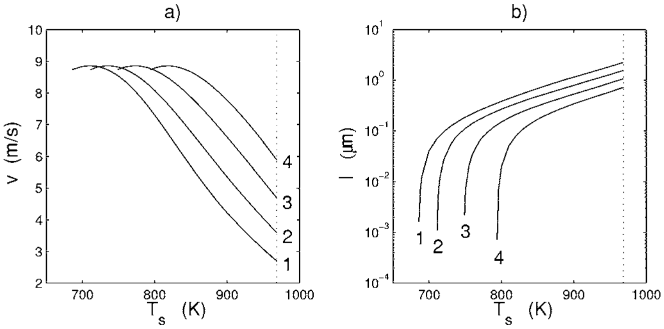

FIG. 11. Speed of a uniformly propagating EC front (a) and melt layer thickness (b) as functions of the substrate temperature T_s for films with different thicknesses: $1-h=3.6$ μm ($\gamma=0.53\times10^6$ s^{-1}), $2-h=1.8$ μm ($\gamma=1.06\times10^6$ s^{-1}), $3-h=0.89$ μm ($\gamma=2.15\times10^6$ s^{-1}), $4-h=0.45$ μm ($\gamma=4.26\times10^6$ s^{-1}).

The results of the computations are shown in Fig. 11 for films with different thicknesses (corresponding to different heat-loss parameters γ). In Fig. 11 one can see that EC fronts mediated by a melt layer can occur only if the substrate temperature T_s exceeds a certain threshold value, T_s^0, corresponding to the left ends of the curves shown in Fig. 11(a). If $T_s < T_s^0$ the melt layer collapses [its thickness l tends to zero, see Fig. 11(b)]. For $T_s > T_s^0$, the frontal speed first slightly grows, reaches a maximum value $v_{\max}$ and then decreases. The value of $v_{\max}$ corresponds to the maximum point of the interface velocity response function $F_c(T_i)$ (see Fig. 10) and does not depend on the heat loss parameter (therefore, it does not depend on the film thickness). Moreover, the maxima on all the curves in Fig. 11 are quite shallow: the difference between the frontal speed corresponding to the threshold substrate temperature T_s^0 and the maximum value $v_{\max}$ is less than 1%. This explains our experimental observations according to which the frontal speed was observed to be practically constant in a wide temperature range and did not depend on the film thickness. For a 1.8 micron film, our computations predict an average frontal speed 8.7 m/s for substrate temperatures in the range 711 K$<T_s<$800 K. For a 0.89 micron film our computations give an average frontal speed 8.8 m/s for substrate temperatures in the range 749 K$<T_s<$800 K. This compares very well with our experimental results described above.

Note that although for $T_s < T_s^0$ sustained uniform propagation of an EC front mediated by a melt layer cannot occur, EC in which the amorphous material is transformed directly into the crystalline phase, without a melt layer, is still possible. This, however, is not described by our model, but is described by the model in Refs. 10 and 11. The characteristic feature of this regime is the increase of the frontal speed with temperature (see Refs. 5, 10, and 11 for details) which explains our experimental observations for EC of a 1.8 micron film for low substrate temperatures 613 K$<T_s<$700 K (see Fig. 4). Thus, the experimentally observed dependence of the EC frontal speed on the substrate temperature that consists of two branches—the one where the EC front speed increases

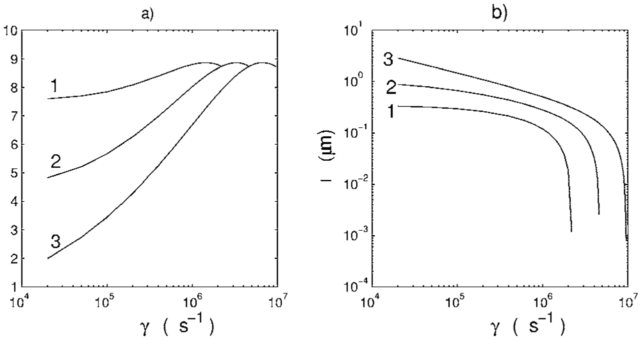

FIG. 12. Speed of a uniformly propagating EC front (a) and melt layer thickness (b) for germanium as functions of the heat loss parameter γ for different substrate temperatures T_s: 1—750 K, 2—800 K, 3—850 K. The parameters are the same as in Fig. 11.

with temperature and the other where it remains essentially constant—can be explained by the two different regimes of EC front propagation: the increasing branch corresponds to EC without melting, governed by a direct amorphous-crystalline transition, and the constant branch corresponds to the melt-mediated EC described by our model. In addition, the transition between the two regimes of explosive crystallization could be a possible cause of the jump in the EC frontal speed observed around $T_s = 700-710$ K (see Fig. 4 and also Ref. 8). We plan to investigate the transition between two EC regimes in greater detail elsewhere.

In the EC regime accompanied by melting, after the substrate temperature exceeds that corresponding to the maximal frontal speed, the latter decreases with a further temperature increase since the melt undercooling decreases. However, this regime was not accessible in our experiments due to multiple nucleation sites that appeared in the film at higher substrate temperatures and prevented the propagation of a planar EC front. Also, obviously, the substrate temperature cannot exceed the melting temperature of the amorphous film T_{ma} that corresponds to the right ends of the curves shown in Fig. 11 and is indicated by the dotted lines.

Figure 11(b) shows the dependence of the melt layer thickness l on the substrate temperature for films with different thicknesses (different heat-loss parameters). One can see that the melt layer thickness increases with the increase of the substrate temperature, and there is a lower threshold for T_s, $T_s = T_s^0$, at which $l \to 0$. This threshold temperature decreases with the decrease of the heat-loss parameter (increase of the film thickness). For the range of T_s used in our experiments described above, the melt layer thickness is in the range from 10 to 100 nm. Such a thickness could not be measured in our experiments but is consistent with other experimental observations.[15] At a fixed substrate temperature, the melt layer thickness increases with the decrease of the heat losses (increase of the film thickness). As one can also see from Fig. 11(a), in the regime where the frontal speed decreases with T_s, the speed is higher for larger heat losses due to the larger melt undercooling (again, this regime was inaccessible in our experiments due to multiple nucleation sites).

Figure 12 shows the dependence of the speed and the melt layer thickness of a uniformly propagating EC front in germanium film as a function of the heat loss parameter γ for three different values of the substrate temperature. One can see that for a given substrate temperature there exists a critical value of the heat loss parameter, γ^0, above which the melt-mediated EC front cannot occur. This corresponds to the right ends of the curves shown in Figs. 12(a) and 12(b). For $\gamma \to \gamma^0$ the melt layer thickness tends to zero, $l \to 0$. However, as discussed above, an EC regime characterized by a direct amorphous-crystalline transformation, not described by our model, is still possible. As one can see from Fig. 12(a), for $\gamma < \gamma^0$, the EC frontal speed exhibits a shallow maximum (i.e., stays almost constant for a certain range of γ) and then decreases with the decrease of γ. Indeed, the decrease of the heat loss coefficient increases the film temperature and decreases the melt undercooling, thus leading to the decrease of the front speed. For the same reason the speed of the front corresponding to a larger substrate temperature is smaller. The melt layer thickness increases monotonically with the decrease of the heat loss parameter [see Fig. 12(b)] and with the increase of the substrate temperature. Note that the dependencies of the frontal speed and the melt layer thickness on temperature shown in Fig. 11 are similar to those obtained in Ref. 6 for explosive crystallization of silicon in ELPE mode.

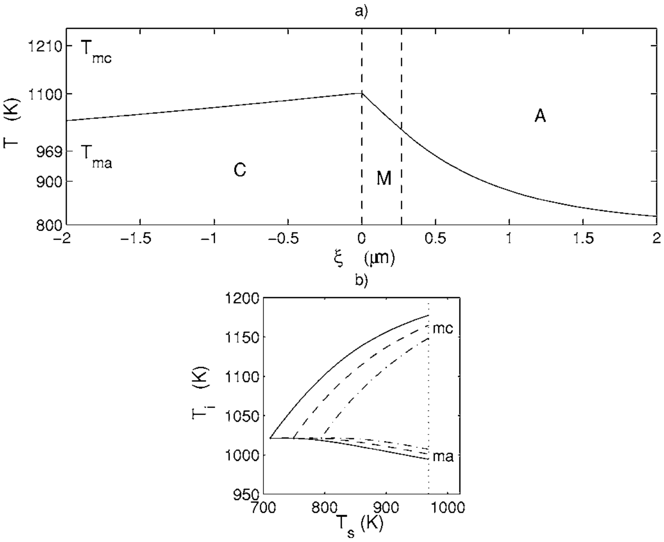

FIG. 13. (a) Temperature profile corresponding to a uniformly propagating EC front in a 1.8-micron germanium film with $T_s = 800$ K. (b) Temperatures at the melt-crystal (mc) and melt-amorphous (ma) interfaces as functions of the substrate temperature, T_s, for films with different thicknesses. Solid line: $h = 1.8$ μm ($\gamma = 1.06 \times 10^6$ s^{-1}), dashed line: $h = 0.89$ μm ($\gamma = 2.15 \times 10^6$ s^{-1}), dashed-dotted line: $h = 0.45$ μm ($\gamma = 4.26 \times 10^6$ s^{-1}).

Figure 13(a) shows a typical temperature profile in a film along which the EC front propagates. It corresponds to the steady state solution (24)–(27) describing a uniformly propagating EC front in a 1.8-micron-thick Ge film. Note that in the particular case shown in Fig. 13 the temperature gradients on the two sides of the interface between the amorphous and melt phases are almost equal: the heat flux difference due to the latent heat of melting is mainly caused by the difference in the thermal conductivities of the two phases.

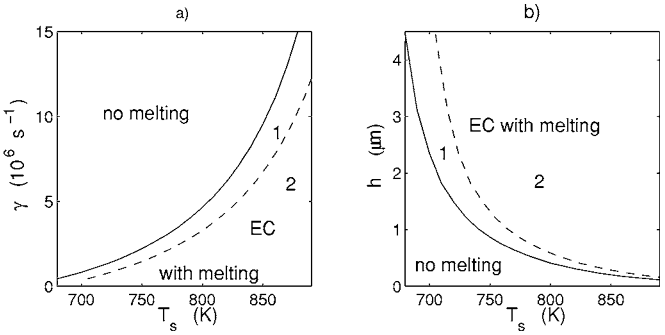

FIG. 14. Regions in the parameter planes, separated by the solid lines, where EC mediated by a melting layer can occur in a germanium film. (a) Substrate temperature: heat loss coefficient, (b) substrate temperature: film thickness (for quartz substrate). Dashed lines: stability boundaries: uniformly propagating planar EC front with melting layer is stable in region 1 and develops the morphological instability in region 2.

Figure 13(b) shows the dependence of the interfacial temperatures at the melt-crystal and melt-amorphous interfaces on the substrate temperature for different values of the heat-loss parameter (different values of the film thickness). Clearly, the temperature at the crystal-melt interface is lower than the equilibrium melting temperature of the crystalline phase while the temperature at the amorphous-melt interface is greater than the equilibrium melting temperature of the amorphous-melt interface. One can see that when the substrate temperature tends to the threshold value T_s^0 corresponding to the collapse of the melt layer, the temperatures of the two interfaces tend to the same constant value. With an increase of the heat-loss parameter, the temperature difference between the two interfaces decreases, corresponding to the decrease of the melt layer thickness.

From the above analysis one can see that EC mediated by a melt layer can occur only if the substrate temperature exceeds a critical value and the heat loss parameter is below a critical value. This allows us to find the boundary in the parameter plane (γ, T_s), as well as in the parameter plane (h, T_s), corresponding to the threshold of melt-mediated EC in germanium. These boundaries are shown in Fig. 14 by the solid lines. Dashed lines show the stability boundaries (see next section).

VI. STABILITY OF THE UNIFORMLY PROPAGATING EC FRONT

A uniformly propagating EC front can become unstable, leading either to oscillations (resulting in a banded structure) or to the formation of cellular or dendritic morphologies. The oscillatory and monotonic instabilities of a uniformly propagating EC front in the absence of a melt layer, when the amorphous phase is transformed directly into the crystalline phase, were studied theoretically in Refs. 10 and 11. In Refs. 7 and 8 morphological instabilities of an EC front in Ge film, that is accompanied by melting of the amorphous phase, were systematically studied experimentally. It was shown that, depending on the substrate temperature and the thickness of the film, the EC front leaves behind various microstructures that can be associated with different kinds of instabilities. One of the observed microstructures consisted of stripes (bands) parallel to the planar front (normal to the front propagation direction), referred to above as a "scalloped" structure. The other type consisted of a cellular structure, i.e., stripes parallel to the front propagation direction (normal to the planar front), referred to above as a "columnar" structure. These two types of microstructure result from two types of EC front instability: the oscillatory instability, leading to frontal speed oscillations and the monotonic (cellular or morphological) instability, respectively. In this section, we shall perform a linear stability analysis of the uniformly propagating EC front, employing parameter values corresponding to Ge films.

Consider perturbations of temperature $\theta_c=\theta_c^{(0)}+\tilde{\theta}_c$, $\theta_m=\theta_m^{(0)}+\tilde{\theta}_m$, $\theta_a=\theta_a^{(0)}+\tilde{\theta}_a$, and interface shapes $\zeta_1=\tilde{\zeta}_1$, $\zeta_2=l+\tilde{\zeta}_2$, where $\tilde{\theta}_{c,m,a}=g_{c,m,a}(\xi)e^{\omega t+ikx}$, $\tilde{\zeta}_{1,2}=H_{1,2}e^{\omega t+ikx}$, where ω and k are the perturbation growth rate and wave number, respectively. Linearize Eqs. (13)–(22) about the uniformly propagating state (24)–(27) to obtain the following equations for the eigenfunctions $g_{c,m,a}(\xi)$ and the growth rate ω:

$$g_c''+Vg_c'-(\omega+\alpha+k^2)g_c=0, \tag{31}$$

$$\chi_m g_m''+Vg_m'-(\omega+\alpha+\chi_m k^2)g_m=0, \tag{32}$$

$$\chi_a g_a''+Vg_a'-(\omega+\alpha+\chi_a k^2)g_a=0, \tag{33}$$

subject to the boundary conditions

$$\xi=0:\ g_c+\frac{d\theta_c^{(0)}}{d\xi}H_1=g_m+\frac{d\theta_m^{(0)}}{d\xi}H_1, \tag{34}$$

$$\omega H_1+\chi_m\left(g_m'+\frac{d^2\theta_m^{(0)}}{d\xi^2}H_1\right)=g_c'+\frac{d^2\theta_c^{(0)}}{d\xi^2}H_1, \tag{35}$$

$$\omega H_1=\left(\frac{df_c}{d\theta}\right)_0\left(g_c+\frac{d\theta_c^{(0)}}{d\xi}H_1\right)-\Gamma_c k^2H_1, \tag{36}$$

$$\xi=l:\ g_m+\frac{d\theta_m^{(0)}}{d\xi}H_2=g_a+\frac{d\theta_a^{(0)}}{d\xi}H_2, \tag{37}$$

$$-q\omega H_2+\chi_a\left(g_a'+\frac{d^2\theta_a^{(0)}}{d\xi^2}H_2\right)=\chi_m\left(g_m'+\frac{d^2\theta_m^{(0)}}{d\xi^2}H_2\right), \tag{38}$$

$$\omega H_2=\left(\frac{df_a}{d\theta}\right)_0\left(g_a+\frac{d\theta_a^{(0)}}{d\xi}H_2\right)+\Gamma_a k^2H_2, \tag{39}$$

where the subscript and superscript 0 relate to the uniformly propagating state and the surface energy parameters $\Gamma_{c,a}$ are

$$\Gamma_c = \delta_c \epsilon_c \exp\left[- e_c \frac{\beta \theta_c^{(0)}(0)}{1 + \beta \theta_c^{(0)}(0)} \right] \times \exp\left[\epsilon_c \left(1 - \frac{\tau_c}{1 + \beta \theta_c^{(0)}(0)} \right) \right], \tag{40}$$

$$\Gamma_a = \delta_a \epsilon_a \exp\left[- e_a \frac{\beta \theta_a^{(0)}(l)}{1 + \beta \theta_a^{(0)}(l)} \right] \times \exp\left[\epsilon_a \left(1 - \frac{\tau_a}{1 + \beta \theta_a^{(0)}(l)} \right) \right]. \tag{41}$$

The solutions of Eqs. (31)–(33) are given by

$$g_c = A e^{\lambda \xi}, \quad g_m = B e^{\xi \mu_+} + C e^{\xi \mu_-}, \quad g_a = D e^{\xi \nu}, \tag{42}$$

where

$$\lambda = \frac{1}{2}[- V + \sqrt{V^2 + 4(\omega + \alpha + k^2)}], \tag{43}$$

$$\mu_\pm = \frac{1}{2\chi_m}[- V \pm \sqrt{V^2 + 4\chi_m(\omega + \alpha + \chi_m k^2)}], \tag{44}$$

$$\nu = \frac{1}{2\chi_a}[- V - \sqrt{V^2 + 4\chi_a(\omega + \alpha + \chi_a k^2)}]. \tag{45}$$

Substituting Eq. (42) into the boundary conditions (34)–(39), one obtains a homogeneous system of linear equations for the constants A, B, C, D, H_1, H_2 that has nontrivial solutions if and only if its determinant $\Delta(\omega, k, p)$ is equal to zero:

$$\Delta(\omega, k, p) = 0. \tag{46}$$

Here, p denotes the set of physical parameters in the problem.

Equation (46) is the dispersion relation that determines the perturbation growth rate ω as a function of the wave number k and the parameters of the system. Equation (46) is rather complicated and cannot be analyzed in the general case. We have computed dispersion curves for the particular cases of 1.8 and 0.89 micron germanium films, which were used in the experiments described above. For the estimate of the surface-energy parameters we have used $\sigma_{\mathrm{mc}} = \sigma_{\mathrm{ma}} = 0.33\ \mathrm{J\ m}^{-2}$. We have found that in a 1.8-micron film a uniformly propagating EC front is stable for substrate temperatures in the range $711\ \mathrm{K} < T_s < 735\ \mathrm{K}$, while for $T_s \geqslant 735\ \mathrm{K}$ it becomes unstable with respect to monotonic perturbations. A uniformly propagating EC front in a 0.89 micron film is stable for $749\ \mathrm{K} < T_s < 773\ \mathrm{K}$ and exhibits a monotonic instability for $T_s \geqslant 773\ \mathrm{K}$. A typical dispersion curve corresponding to this type of instability is shown in Fig. 15. One can see that there is a preferred wave number k_* corresponding to the maximum growth rate. Such an instability will result in periodic modulations of the frontal shape along the front with the characteristic wavelength $\Lambda_* = 2\pi / k_*$. Since the front moves through the film, this instability will leave behind a striped pattern, periodic in the direction along the front (normal to the front propagation) which is the "columnar structure" seen in experiments. We have computed the wavelength Λ_* of the columnar structure and the characteristic time $\tau_* = 1/\omega_{\max}$ of the instability development in a 1.8 micron film for different substrate temperatures. The results are shown in Table II. One can see that the typical wavelength of the columnar structure is a few microns, which is in qualitative agreement with experimental observations shown in Table I. Also, the theory predicts that the wavelength of the columnar structure decreases with the increase of the substrate temperature which is also in agreement with experiment. However, one can see that the computed wavelength is a few times smaller than the average steady state width of "crystal columns" measured in experiments. This can be explained by the fact that the linear stability theory predicts the preferred wavelength only at the beginning of the instability development (initial stage of the perturbation growth) and does not describe the established steady-state wavelength during the strongly nonlinear stage of the instability. At the same time, as mentioned above, the columnar structure wavelength at the very beginning of the front propagation was indeed observed to be considerably smaller than in the steady-state. The characteristic time of the instability development for $T = T_s > 738$ K is less than 10 ms and decreases with the increase of T_s. This is much less than the characteristic time of front propagation through the film so that the formation of the columnar structure is seen at the initial stage of front propagation, which is consistent with experimental observations.

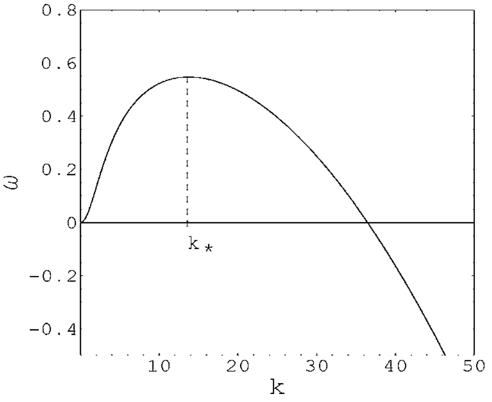

FIG. 15. Dispersion curve $\omega(k)$ (dimensionless) for a 1.8-micron-thick germanium film with $T_s = 740$ K.

We have also computed the stability boundary for a uniformly propagating, melt-mediated EC front in germanium film as a function of the substrate temperature and the heat loss coefficient [see dashed line in Fig. 14(a)] and for the

TABLE II. Characteristic wavelength and characteristic time of morphological instability of a planar EC front in a 1.8-micron-thick germanium film for different substrate temperatures.

T_s K	Λ_*, μm;	τ_*, μs
736	4.0	51
738	2.3	7.0
740	1.8	3.4
750	1.1	0.8

quartz substrate—as a function of the substrate temperature and the film thickness [see dashed line in Fig. 14(b)]. Region 1 corresponds to stable front propagation, region 2 corresponds to the morphologically unstable front. One can see that the interval of substrate temperatures corresponding to stable propagation of the EC front is almost the same for different values of the heat loss coefficient and the film thickness. However, with the increase of T_s, the interval of heat loss coefficients corresponding to stable front propagation increases considerably, while the interval of the corresponding film thicknesses considerably decreases.

Note too, that we have not found any oscillatory instability in this system, i.e., no complex-conjugate roots of Eq. (46) with positive real part. This is consistent with the experimental observations described above in which the scalloped structure was observed for parameter values for which our theory predicts the absence of EC mediated by melting. Therefore, the scalloped structure observed in our experiments is likely a result of the oscillatory instability of the EC front without melting, governed by the direct amorphous-crystalline transition, which is not described by our model. At the same time, as shown in Refs. 10 and 11 the oscillatory instability is typical of EC governed by a direct amorphous-crystal phase transformation. Therefore, the scalloped structure in EC germanium film observed in Ref. 8 is also likely a result of the oscillatory instability of an EC front governed by the direct transition from the amorphous to the crystalline state.

The dispersion relation (46) is a rather complicated function of ω and k that depends on many parameters, so the general stability analysis of EC front propagation in the presence of melting is rather difficult. In a special case, however, it is possible to significantly simplify the dispersion relation. Specifically, if the thermal conductivities of the amorphous, melt, and crystalline phases do not significantly differ from one another, the interface response functions are assumed to be linear (which is a reasonable approximation for melt-mediated EC), surface energy is neglected, and the dimensionless thickness of the melt layer is small, $l \ll 1$. Then the dispersion relation (46) can be greatly simplified by assuming $\chi_a = \chi_m = 1$ and by taking the limits $l \to 0$, and $\Gamma_{a,c} \to 0$. The resulting dispersion relation will yield results which may only be qualitatively, but not quantitatively correct, since the conditions for the simplification are not necessarily met in practice. Nevertheless, it is instructive to carry out the analysis, which yields insight into the stability behavior. In this case, the uniformly propagating EC front is described by Eqs. (24)–(26) with Eq. (28) so that the dispersion relation (46) reduces to

$$\Gamma(\omega - f_a'\theta_a')(\omega - f_c'\theta_c') + q f_a'(\omega - f_c'\theta_c')(\omega - V\lambda_-) - f_c'(\omega - f_a'\theta_a')(\omega - V\lambda_+) = 0, \tag{47}$$

where $\lambda_\pm = (-V \pm \Gamma)/2$, $\Gamma = \sqrt{V^2 + 4(\omega + \alpha + k^2)}$, $f_c' = (df_c/d\theta) = \text{const}$, $f_a' = (df_a/d\theta) = \text{const}$, $\theta_c' = r_+ A_e$, $\theta_a' = r_- A_e$, $A_e = (1-q)V/\Gamma_0$, $\Gamma_0 = \sqrt{V^2 + 4\alpha}$.

Equation (47) can be analyzed in the case of long-wave perturbations, whose wavelength Λ is much larger than the characteristic width of the thermal boundary layer $l_0 = \lambda_c/(\rho c_f v_0)$. This corresponds to the limit $k \to 0$ in Eq. (47). In this limit, the dispersion relation (47) yields $\omega = \frac{1}{2}(\partial^2\omega/\partial k^2)_{k=0} k^2 + \cdots$, and the EC front is unstable with respect to long-wave perturbations if $(\partial^2\omega/\partial k^2)_{k=0} > 0$. One obtains

$$\left(\frac{\partial^2\omega}{\partial k^2}\right)_{k=0} = \frac{2}{\Delta} f_a' f_c'(q-1) \times V^2[V(1-q) + (1+q)\Gamma_0],$$

$$\Delta = \Gamma_0^4\left[f_a'\left(1 + \frac{V}{\Gamma_0}\right) + q f_c'\left(1 - \frac{V}{\Gamma_0}\right)\right] + 4\alpha f_a' f_c'[\Gamma_0(q^2-1) - V(q-1)^2]. \tag{48}$$

It is easy to show that $(\partial^2\omega/\partial k^2)_{k=0} > 0$ for $q > 1$. Thus, in this approximation the EC front is unstable with respect to long-wave perturbations if the latent heat of melting of the amorphous phase is larger than that of the crystalline phase. This conclusion has a simple qualitative explanation. Indeed, the mechanism of EC front propagation in the presence of melting is due to the heat released at the melt-crystal interface which is absorbed at the melt-amorphous interface. If a protrusion is formed at the crystal-melt interface the heat flux from the protrusion toward the melt-amorphous interface increases and is absorbed at the melt-amorphous interface due to the greater latent heat of melting. This cools the melt further and leads to growth of the protrusion, i.e., to instability. In contrast, if the latent heat of melting of the amorphous phase is smaller than that of the crystal phase ($q < 1$), the heat flux from the crystal-melt protrusion cannot be completely absorbed at the melt-amorphous interface, leading to heat accumulation in the melt layer and to melting of the protrusion. Thus, the planar crystal-melt interface is stable in this case. Germanium corresponds to $q < 1$. We can show that if the heat loss parameter α is sufficiently small the expression (48) is negative so that the propagating EC front is stable, though it may not be stable for larger α. Though the simplified criterion has a certain appeal due to its simple physical interpretation, it does not necessarily hold in the general case.

VII. NONLINEAR EVOLUTION OF THE MORPHOLOGICAL INSTABILITY

In this section we derive a nonlinear evolution equation that describes the behavior of a morphologically unstable EC front near the instability threshold. The derivation is performed by means of a standard multiple scale analysis, the details of which can be found, e.g., in Ref. 16. Here we describe the main steps in deriving the weakly nonlinear evolution equation.

We consider the parameters of the system to be such that the EC front is weakly unstable (near the instability threshold) so that the dispersion relation can be expanded as

$$\omega = ak^2 - bk^4, \tag{49}$$

where

$$a=\frac{1}{2}\left(\frac{\partial^2\omega}{\partial k^2}\right)_{k=0}=O(\epsilon^2), \quad b=\frac{1}{24}\left(\frac{\partial^4\omega}{\partial k^4}\right)_{k=0}=O(1).$$

Here, the small parameter $\epsilon \ll 1$ is proportional to $\sqrt{P-P_c}$, where the parameter P stands for any of the parameters in the problem, e.g., α, and P_c is the critical value of P corresponding to the onset of the instability. Indeed, ϵ may be defined by $\epsilon^2=(P-P_c)/P_c$. In this case the range of the wavenumbers Δk corresponding to the unstable modes ($\omega > 0$, see Fig. 12) is small, $\Delta k \sim \epsilon \ll 1$, and the maximal growth rate $\omega_{\max} \sim \epsilon^4$.

We introduce the long-scale coordinate along the front $X=\epsilon x$, and the slow time variable $\tau=\epsilon^4 t$, and consider perturbations of the temperature field in the three phases and perturbations of the two planar interfaces of a uniformly propagating EC front in the form of the expansions

$$\theta \sim \theta^{(0)}(\xi)+\epsilon^2\theta^{(1)}(\xi,X,\tau)+\epsilon^4\theta^{(2)}(\xi,X,\tau)+\epsilon^6\theta^{(3)}(\xi,X,\tau) + \cdots, \tag{50}$$

$$\zeta_1 \sim \epsilon^2\zeta_1^{(1)}(X,\tau)+\epsilon^4\zeta_1^{(2)}(X,\tau)+\epsilon^6\zeta_1^{(3)}(X,\tau)+\cdots, \tag{51}$$

$$\zeta_2 \sim l+\epsilon^2\zeta_2^{(1)}(X,\tau)+\epsilon^4\zeta_2^{(2)}(X,\tau)+\epsilon^6\zeta_2^{(3)}(X,\tau)+\cdots. \tag{52}$$

Substituting the expansions (50)–(52) into the problem (13)–(22), one obtains a sequence of linear problems in even orders of the small parameter ϵ. The solvability condition of the problem at order ϵ^2 gives

$$\begin{pmatrix}\zeta_1\\ \zeta_2\end{pmatrix}=\begin{pmatrix}\beta_1\\ \beta_2\end{pmatrix}U(X,\tau), \tag{53}$$

where β_1 and β_2 are the components of the eigenvector of the linearized problem (13)–(22) as $k\to 0$, and $U(X,T)$ is an as yet unknown function. The solvability condition for the problem at order ϵ^4 gives the condition for the instability threshold, $2a=\partial^2\omega/\partial k^2=0$, and is identically satisfied since the parameters have been chosen such that $a=O(\epsilon^2)$. The solvability condition for the problem at order ϵ^6 gives the following evolution equation for the function $U(X,\tau)$,

$$U_\tau + aU_{XX} + bU_{XXXX} - \frac{V}{2}(U_X)^2 = 0. \tag{54}$$

where a and b are defined in Eq. (49), and V is the dimensional speed of the propagating planar EC front.

Equation (54) is the well-known Kuramoto-Sivashinsky (KS) equation that describes weakly nonlinear evolution in many systems with translation invariance characterized by a monotonic instability with the long-wave spectrum (49),[17] such as the thermo-diffusive instability of a flame front[18] or the instability of waves on liquid films flowing down an inclined plane.[19] It has been extensively studied (see, e.g., Ref. 20) and is known to exhibit cellular structures which vary slowly in time and space in a chaotic manner. In our case, it describes the nonlinear evolution of an unstable EC front near the instability threshold, when the perturbation wavelength is large compared to the width of the thermal boundary layer at the moving front. The solution of this equation describes the shape of the front, i.e., the shape of the two interfaces given by Eq. (53). One can show that the two components of the eigenvector in Eq. (53) have the same sign so that the perturbations of the two interfaces are always in phase. Indeed, when the crystal-melt interface is corrugated, the heat flux due to the latent heat of crystallization is larger at the protrusions of the crystal-melt interface; this leads to the increased melting of the adjacent parts of the melt-amorphous interface that, therefore, exhibits the same corrugated shape. An example of such a shape appears in Fig. 16(b) which shows the solution of the KS equation at a particular moment of time. When such a morphologically unstable EC front propagates along the film, it leaves behind a microstructure in which the spatiotemporal evolution of the frontal shape is imprinted. An example of spatiotemporal evolution described by the (scaled) KS equation is shown in Fig. 16. One can see that the spatiotemporal pattern described by the KS equation is very similar to the columnar structure observed in our experiments.

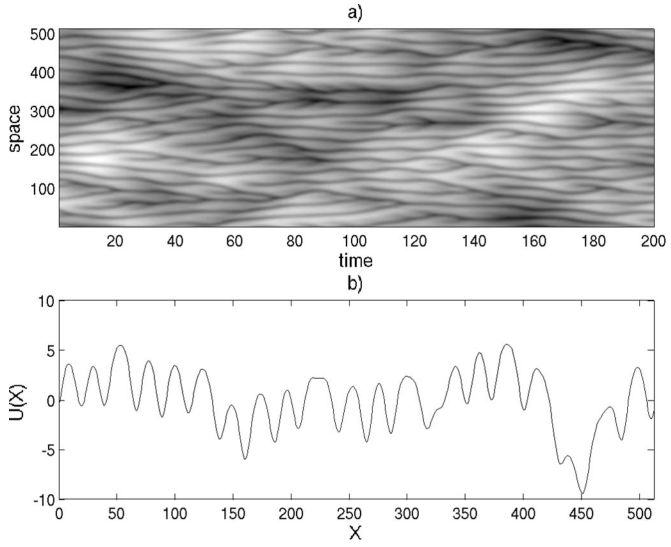

FIG. 16. Solution of the rescaled KS equation (54) (for $a=b=V=1$) describing the shape of the EC front near the morphological instability threshold. (a) Spatiotemporal diagram which is similar to the columnar structure. (b) Solution describing the frontal shape at a particular moment of time.

VIII. SUMMARY

We have studied explosive crystallization accompanied by melting (ELPE mode) in a thin film of amorphous material, both experimentally and theoretically. In this regime, a thin layer of melt between the amorphous and crystalline phases is formed. The melt is undercooled with respect to the crystalline phase and overheated with respect to the amorphous phase. Melt crystallization at the crystal-melt interface releases the latent heat that melts the amorphous phase. This process can lead to self-propagation of the EC front that consists of two interfaces—crystal-melt and melt-amorphous, with a melt layer between them. The melt-mediated EC front propagates through the amorphous film and transforms it into the crystal (polycrystalline) film.

We have performed experiments using films of amorphous germanium. Laser-induced, linear EC fronts, uniformly propagating over large distances have been achieved in films with various thicknesses deposited on a quartz substrate. Depending on the front speed, the film thickness and the substrate temperature, different types of morphology of the resulting crystal phase have been observed: columnar, scalloped, and mixed.

We have developed a theory of explosive crystallization in thin amorphous films, accompanied by melting. Our theory predicts the speed of a uniformly propagating EC front mediated by a layer of melt, the melt layer thickness, the critical value of the substrate temperature above which front propagation is possible, as well as the critical value of the heat loss parameter (film thickness) above (below) which the melt-mediated EC front cannot propagate. The results of our analysis and computations are in good agreement with experimental observations. We have argued that while for certain ranges of substrate temperatures and film thicknesses, melt-mediated EC front propagation cannot occur, an EC front governed by a direct, amorphous-crystal phase transformation is still possible. This argument is supported by our experimental observations.

We have performed a linear stability analysis of a uniformly propagating EC front in the presence of a melt layer. We have shown that the front can exhibit a monotonic cellular instability which is similar to the Mullins-Sekerka instability of solidification fronts. We have found the range of substrate temperatures for which the instability occurs and have computed the wavelength of the most rapidly growing mode. Our predictions are in good agreement with our experimental observations. Also in agreement with our experimental observations is our theoretical result that does not show the presence of an oscillatory instability for a uniformly propagating EC front mediated by a melt layer. We therefore argue that the scalloped microstructure of a crystal phase observed in experiments results from an oscillatory instability of the EC front that is governed by a direct amorphous-crystal phase transformation, with no melting. Previous analysis of the stability of EC fronts in this mode supports our conclusion.

An interesting feature observed in the experiments that remains unexplained is the transitional regime that leads to the formation of a mixed microstructure, somewhat between the scalloped and the columnar microstructures. We conjecture that this regime could result from the coexistence of two regimes of the EC front propagation: with and without melting, that can occur simultaneously on different parts of the front. This, however, requires further investigation.

In conclusion, we note that there are several effects, not considered in the present paper, that can affect the nature of the EC front instability and the wavelength selection process. One is the effect of impurities that might be present in the amorphous film. The presence of impurities will change the equilibrium melting and crystallization temperatures, thus affecting the EC front propagation speed and the stability conditions. Also, the concentration of impurities in the melt layer can provide an additional instability mechanism, similar to the morphological instability during the crystallization of binary alloys; the dependence of the melting and crystallization kinetic parameters on the impurity concentration can yield an oscillatory instability.[12] Another effect is associated with elastic stress generated in a thin film during its explosive crystallization on a solid substrate.[21–23] The elastic stress can change the kinetic parameters of the phase transformation,[24–26] thus changing the EC front stability conditions and possibly leading to a new type of instability. We plan to investigate these effects in the future.

ACKNOWLEDGMENTS

This work was supported by NSF Grant No. CTS-0431431. The authors are grateful to Oscar D. Dubon of the Department of Materials Science and Engineering, University of California, Berkeley, for his help in fabricating and characterizing the samples.

---

[1] T. Choi, D. J. Hwang, and C. P. Grigoropoulos, Opt. Eng. **42**, 3383 (2003).

[2] M. Lee, S. Moon, M. Hatano, and C. P. Grigoropoulos, J. Appl. Phys. **88**, 4994 (2000).

[3] M. Lee, S. Moon, M. Hatano, and C. P. Grigoropoulos, Appl. Phys. A **73**, 317 (2001).

[4] B. G. Bagley and H. S. Chen, in *Laser-Solid Interactions and Laser Processing 1978*, edited by S. D. Ferris, H. J. Leamy, and J. M. Poate, AIP Conf. Proc. (AIP, New York, 1979), pp. 97–101.

[5] V. A. Shklovskii and V. M. Kuz'menko, Sov. Phys. Usp. **32**, 163 (1989).

[6] H.-D Geiler, E. Glaser, G. Gotz, and M. Wagner, J. Appl. Phys. **59**, 3091 (1986).

[7] A. P. Chojnacka, Ph.D. thesis, Cornell University, Cornell, 2002.

[8] A. Chojnacka and M. O. Thompson, in *Growth, Evolution and Properties of Surfaces, Thin Films and Self-Organized Structures*, edited by S. C. Moss, D. B. Poker, and D. Ila, Mater. Res. Soc. Symp. Proc. (Materials Research Society, Warrendale, 2001), p.11.12.1-8.

[9] E. J. Albenze, M. O. Thompson, and P. Clancy, Phys. Rev. B **70**, 094110 (2004).

[10] W. van Saarloos and J. D. Weeks, Phys. Rev. Lett. **51**, 1046 (1983); Physica D **12**, 279 (1984).

[11] D. A. Kurtze, W. van Saarloos, and J. D. Weeks, Phys. Rev. B **30**, 1398 (1984); D. A. Kurtze, Physica D **20**, 303 (1986).

[12] S. H. Davis, *Theory of solidification* (Cambridge University Press, Cambridge, 2001).

[13] S. G. Tomlin, E. Khawaja, and G. K. M. Thutupalli, J. Phys. C **9**, 4335 (1976).

[14] P. Germain, K. Zellama, S. Squelard, and J. C. Bourgoin, J. Appl. Phys. **50**, 6986 (1979); M. D. Kluge and J. R. Ray, Phys. Rev. B **39**, 1738 (1989); P. A. Stolk, A. Polman, and W. C. Sinke, *ibid.* **47**, 5 (1993).

[15] F. Vega, R. Serna, and C. N. Alfonso, J. Appl. Phys. **75**, 7287 (1994); F. Vega, J. Solis, J. Siegel, and C. N. Alfonso, *ibid.* **88**, 6321 (2000); F. Vega, N. Chaoui, J. Solis, J. Armengol, and C. N. Alfonso, *ibid.* **97**, 103519 (2005).

[16] B. J. Matkowsky and G. I. Sivashinsky, SIAM J. Appl. Math. **37**, 686 (1979); A. A. Nepomnyashchy, Physica D **86**, 90 (1985).

[17] Y. Kuramoto, Prog. Theor. Phys. **54**, 687 (1975).

[18] G. I. Sivashinsky, Acta Astronaut. **4**, 1177 (1977).

[19] A. A. Nepomnyashchy, Fluid Dyn. **9**, 354 (1974).

[20] T. Bohr, M. H. Jensen, G. Paladin, and A. Vulpiani, *Dynamical System Approach to Turbulence* (Cambridge University Press, Cambridge, 1998).

[21] K. H. Heinig and H.-D. Geiler, Phys. Status Solidi A **92**, 421 (1985).

[22] V. I. Emelyanov and I. M. Panin, Appl. Phys. A **57**, 561 (1993).

[23] V. I. Emelyanov and A. A. Soumbatov, Phys. Status Solidi A **158**, 493 (1996).

[24] M. J. Aziz, P. C. Sabin, and G. Q. Lu, Phys. Rev. B **44**, 9812 (1991); W. Barvosa-Carter, M. J. Aziz, L. J. Gray, and T. Kaplan, Phys. Rev. Lett. **81**, 1445 (1998).

[25] G. Grinstein, Y. Tu, and J. Tersoff, Phys. Rev. Lett. **81**, 2490 (1998); J. Tersoff, Y. H. Tu, and G. Grinstein, Appl. Phys. Lett. **73**, 2328 (1998).

[26] A. Pumir and V. V. Barelko, Eur. Phys. J. B **16**, 137 (2000).